

Research Article

Vibrational Characteristics of Au-Doped Si Nanowires: A Molecular Dynamics Study with a Modified Embedded Atom Method Potential Developed for Si-H-Au Systems

Bin Liu ¹, Yun'an Zhang ², Xinfeng Wang ¹, Yanjiao Li ¹, and Yingjuan Yue ¹

¹Department 403, Rocket Force University of Engineering, Xi'an 710038, China

²Laboratory of Science and Technology on Integrated Logistics Support, National University of Defense Technology, Changsha 410000, China

Correspondence should be addressed to Bin Liu; liubinbin19880108@163.com

Received 17 February 2022; Accepted 10 September 2022; Published 30 September 2022

Academic Editor: Anuja Datta

Copyright © 2022 Bin Liu et al. This is an open access article distributed under the Creative Commons Attribution License, which permits unrestricted use, distribution, and reproduction in any medium, provided the original work is properly cited.

Silicon nanowires (SiNWs) are promising structures as resonators for applications in ultrasensitive force and mass transducers. In the present work, large-scale molecular dynamics simulations were conducted to explore the effect of gold (Au), a commonly used catalyst, on the vibrational properties of [1 0 0] and [1 1 0] SiNWs. The force field was established using the modified embedded atom method (MEAM) formalism. The parameterization focused on the properties of the hydrogen-covered SiNWs doped with Au, involving the formation energy as well as the structural and vibrational characteristics. The vibrational characteristics of a clamped-clamped SiNW were examined through excitation using a sinusoidal velocity field after energy minimization and thermal equilibration. Different doping concentrations and distributions can significantly change the frequency response, quality factor Q , and beat phenomenon. The natural frequency f_0 decreased with increasing Au concentration, whereas the effect of the impurity distribution on f_0 was negligible. Furthermore, Q was sensitive to the Au concentration and distribution, and the increased concentration led to an overall increment in Q , accompanied by considerably increased scattering. Besides, the beat period of [1 1 0] SiNWs showed a strong positive correlation with the concentration. The vibration along the elementary axes cannot produce the beat phenomenon. Deflection of the elementary axes in a very small range would lead to a higher energy dissipation rate. In addition, owing to the considerable difference between the atomic masses of Au and Si, randomly distributed Au atoms significantly disturb the symmetry of the SiNWs. However, the elementary axes of the [1 1 0] SiNWs remained stable, even in the models with extremely radial or longitudinal impurity segregation. In contrast, we failed to capture the distinguishable elementary axes for most of the doped [1 0 0] samples. The features described above indicate that the impurity Au can effectively tune the resonant frequency of the [1 0 0] SiNWs, meanwhile, causes no large frequency shift that could be potentially caused by the deflection of the elementary coordinate system.

1. Introduction

The distinctive properties, including surface effects, quantum effects, and electro-optic properties, facilitate nanowires (NW) to be widely applied in critical domains, such as biosensing, thermoelectrics, and new generation lithium batteries. Size reduction leads to outstanding natural frequencies in the range of GHz to THz and excellent energy efficiency; hence, they are used as key structures in ultrasensitive mass [1] and force [2] transducers.

The influence of impurities on the vibrational characteristics of NWs is a topic of research interest. Zhao et al. [3] found that rare metal elements can modulate the sensitivity of ZnO nanowires. Islam et al. [4] systematically studied how the guest element distribution governed by grading functions modifies the mechanical and vibrational properties of functionally graded Cu-Ni NWs. Georgakaki et al. [5] investigated the effects of the Si percentage on the natural frequency f_0 and quality factor Q in $\text{Si}_x\text{Ge}_{1-x}$ and $\text{Si}/\text{Si}_x\text{Ge}_{1-x}$ nanowires. To be strict, the minor functional elements in the

above studies are not impurities because they are intentionally introduced. To date, we have not found any other reports on the effects of impurities on the vibrational performance of SiNWs. In the fabrication processes of SiNWs, impurities, such as metal catalysts in the bottom-up procedure and high-energy ions in the top-down procedure, are introduced inevitably. Therefore, this study investigated how the dissolving Au [6], commonly used for catalyzing the unidirectional growth of SiNWs [7], modulates the vibrational properties of SiNWs.

Studies on the vibrational characteristics of SiNWs mainly focus on f_0 and Q . SiNWs vibrate near f_0 when functioning as resonators, and a sufficiently high Q is required to ensure the accuracy of force and mass detection. Experimental, analytical, and numerical studies addressing these aspects have emerged in recent years. Technical parameters, including vibration modes and their corresponding frequencies [8] and Q determined experimentally, are used to evaluate the vibrational performance of SiNWs. In addition, experimental measurements can be used to control the cubic nonlinearity of SiNW resonators [9]. On the analytical front, the mathematical models developed based on continuum theory can calculate the f_0 of an NW with surface effects [10] and characterize the nonlinear vibration influenced by surface stress [11]. Numerical simulations can accomplish the abovementioned tasks with appropriate initial excitation [4, 5, 12, 13]. Compared with analytical methods, numerical methods, e.g., molecular dynamics (MD), are advantageous because they offer flexibility for structural modeling for non-ideal NWs. In other words, NWs with internal or surface defects are in line with physical reality. Obviously, numerical methods are more economical and can also extract vibrational features without external noise disturbance. Besides, time-dependent properties and kinetic relationships are beyond the scope of the former two methods. However, in numerical simulations, the force field used to describe the behaviors of an NW should be sufficiently reliable.

In this study, large-scale MD was used to investigate the vibrational characteristics of Au-doped [1 0 0] and [1 1 0] SiNWs. The influences of the impurity concentration and distribution on the frequency response, Q , and beat phenomenon were systematically investigated. This paper is divided into two sections. The first section presents the optimization of the parameter sets for the Si-H-Au ternary MEAM potential and the reliability validation. The second section explains the simulation results and phenomena in detail.

2. Parameterization of the MEAM Potential for the Si-H-Au Ternary System

This work employed the second-nearest MEAM (2NN MEAM), and its mathematical scheme is briefly introduced in an earlier Ref. [14]. The 2NN MEAM has been successfully applied to describe metals, semiconductors, and gas elements, and it possesses excellent scalability for multielement systems [15]. It also provides a good description of the Si surface properties [16], which are especially important for

this work. We did not choose the state-of-the-art surrogate model [17, 18] fitted by machine learning; although, it is more accurate and has outstanding transferability. More importantly, it is several orders more computationally expensive and thus is not suitable for dynamic processes in nanoseconds. All empirical models are confined to Newtonian classical mechanics, which cannot accurately predict all properties of a particular material. In particular, when the simulations involve bond breaking and recombination, the credibility of the empirical potentials is questionable. Therefore, the SiNWs were allowed to vibrate only in the elastic range.

There are several studies on the MEAM potentials for Si-Au binary systems. Ryu and Cai [6] fitted the parametric set for Si-Au MEAM potential based on the binary phase diagram, which was used to simulate the growth of SiNWs catalyzed by Au. Kuo and Clancy [19] optimized the MEAM potential according to several hypothetical Si-Au compounds, and it was applied to simulate the evolution of the Si-Au interface. Empirical potentials can be optimized for a particular simulation scenario. In this study, the vibrational characteristics of Au-doped SiNWs were highlighted. The theoretical expression of the natural frequency of a clamped-clamped NW is given below:

$$f_n = \frac{\omega_n}{2\pi L^2} \sqrt{\frac{EI}{\rho A}}, \quad (1)$$

where the length L and moment of inertia I are determined by the size and cross-sectional shape of the NW. ω_n is the eigenvalue of the characteristic equation $\cos \sqrt{\omega_n} \cosh \sqrt{\omega_n} = 1$. From the simplest perspective, impurities modulate the natural frequency by changing the elastic modulus E and density ρ . ρ is determined by the impurity concentration, whereas E is mainly related to elastic constants and lattice distortion. Following the above guideline, the 2NN MEAM potential was optimized in this work. In addition, MD can only deal with thin NWs (<20 nm). The scale that can be handled is smaller owing to the complexity in the formalism of the MEAM. H atoms often terminate the surface of an ultrathin NW after removing the surface oxide with HF [20]. Therefore, the Si-H-Au ternary system is considered to guarantee that our models are in line with engineering specimens.

Several versions of the MEAM model have been developed. This work used the common formalism [21] to calculate the energy as follows:

$$E = \sum_i \left[F_i(\bar{\rho}_i) + \frac{1}{2} \sum_{j \neq i} \phi(R_{ij}) \right]. \quad (2)$$

The first term is the embedding energy for atom i with background electron density $\bar{\rho}_i$. The second term describes the pair interaction, which is the sum over all neighbors j of i within the cutoff distance. The following equation was chosen to calculate the background electron density $\bar{\rho}_i$.

TABLE 1: MEAM parameters for Si, H, and Au. The units of cohesive energy E_c and bulk modulus B are eV and GPa, respectively. The cutoff distance is 6 Å.

Ele. ^a	E_c	α	B	$\beta^{(0)}$	$\beta^{(1)}$	$\beta^{(2)}$	$\beta^{(3)}$	A	$t^{(1)}$	$t^{(2)}$	$t^{(3)}$	C_{\min}	C_{\max}	d_{attrac}	d_{repu}	ρ_0
Si [16]	4.63	4.90	99	3.55	2.50	0	7.50	0.58	1.80	5.25	-2.61	1.42	2.80	0	0	1
H [22]	2.225	2.96	0.74 ^c	2.96	3.00	3.00	2.50	2.50	0.20	-0.10	0.00	2.00	2.80	0	0	20.5
Au ^b	3.93	6.60	180	4.99	4.68	4.00	-2.19	1.32	5.90	3.29	16.46	2.00	2.80	0	0.066	0.48

^aThe reference structures of unary Si, H, and Au are diamond, dimer, and face-centered cubic (FCC), respectively. ^bDeveloped in this work. ^cThe distance between H atoms in a dimer instead of the bulk modulus.

TABLE 2: MEAM predictions of the lattice constant a_0 (Å), elastic constants C_{ij} (GPa), formation energy of vacancy (eV), surface energies (eV), and structural energy differences $E_{\text{FCC/BCC}}$ and $E_{\text{FCC/HCP}}$ (eV), in comparison with experimental values and higher-level calculations. The energies of vacancy formation and surface are obtained after relaxation.

Properties	Expt.	First-principle	Tight-binding	MEAM	
				Others	This work
a_0	4.07 ^e	4.068 ^e , 4.079 ^c	—	4.073 ^e	4.078
C_{11}	201.63 ^a	217 ^b , 187 ^c	—	201.5 ^b	204.75
C_{12}	169.67 ^a	171 ^b , 168 ^c	—	169.7 ^b	167.20
C_{44}	45.44 ^a	47 ^b , 37 ^c	—	45.4 ^b , 38 ^d	42.02
B	180.32 ^a	174 ^c	—	—	179.72
E_v	0.89 ± 0.04 ^d	0.55 ^b	0.49 ^d	0.91 ^b , 0.7 ^d	0.89
$\gamma_{(100)}$	1.54 ^b	1.97 ^b	1.54 ^d	1.08 ^b , 0.95 ^d	1.55
$\gamma_{(110)}$	—	1.10 ^b	1.85 ^d	1.05 ^b , 1.00 ^d	1.83
$\gamma_{(111)}$	—	0.92 ^b	1.48 ^d	0.90 ^b , 0.70 ^d	1.42
$E_{\text{FCC/BCC}}$	—	—	0.019 ^d	0.02 ^d	0.18
$E_{\text{FCC/HCP}}$	—	—	0.0086 ^d	0.021 ^d	0.09

^a[24], 0 K values extrapolated from smooth curves, which are determined experimentally. ^bValues calculated in Ref. [23] or quoted therein. ^cDensity functional theory (DFT) calculations in this work. ^dValues calculated in Ref. [19] or quoted therein. ^eValues calculated in Ref. [25] or quoted therein.

$$\bar{\rho}_i = \rho_i^{(0)} \frac{2}{1 + \exp(-\Gamma_i)}, \quad (3)$$

where $\rho_i^{(0)}$ is the spherically symmetric partial term, and Γ_i is the angular dependence. The left mathematical description of the MEAM potential is in line with Ref. [15].

Table 1 summarizes the MEAM parameters of elements Si, H, and Au. The sets for Si and H were extracted from earlier publications [16, 22], respectively.

2.1. MEAM Potential for Au. Several available MEAM potentials for Au [6, 19, 22, 23] were not chosen for our work, as the parameters had to be optimized for obtaining better predictions of the fundamental properties of the Si-Au binary system. The properties referred for optimizing the Au unary MEAM potential include lattice constant, elastic constants, surface energy, and formation energy of vacancies. The MEAM values of these properties are satisfactory, as shown in Table 2. The experimental datum of the (1 0 0) surface energy was considered in the fitting. Therefore, the MEAM prediction showed that the energy of the (1 0 0) surface was much lower than that of the (1 1 0) surface. This is inconsistent with the first principle calculations but agrees with the tight-binding calculations. In addition, the MEAM

TABLE 3: MEAM parameters of Si-Au, Si-H, and Au-H binary systems. The units of cohesive energy E_c and nearest neighbor distance r_e are eV and Å, respectively. Refer to [15] for the definition of each parameter.

Parameter	Si-Au	Si-H	H-Au
Reference structure	b1-SiAu	Diamond-SiH	Dimer-HAu
E_c	5.65	3.49	2.20
r_e	1.85	1.585	1.50
α	2.133	2.774	3.990
C_{\min} (A-B-A)	2.00	2.20	2.00
C_{\min} (A-A-B)	2.00	1.00	2.00
C_{\min} (A-B-B)	2.00	1.00	2.00
C_{\min} (B-A-B)	2.00	2.00	2.00
C_{\max} (A-B-A)	3.80	3.50	2.80
C_{\max} (A-A-B)	2.50	3.80	2.80
C_{\max} (A-B-B)	2.80	2.80	2.80
C_{\max} (B-A-B)	2.80	2.80	2.80
d_{attrac}	0	0	0.18
d_{repu}	0	4.25	-0.015

TABLE 4: Comparisons of the lattice constant a_0 (Å), cohesive energy E_c (eV), and elastic constants C_{ij} (GPa) between Si₇Au and Si.

	a_0		E_c		C_{11}		C_{12}		C_{44}		B	
	DFT	MEAM	DFT	MEAM	DFT	MEAM	DFT	MEAM	DFT	MEAM	DFT	MEAM
Si	5.44	5.43	4.49	4.63	157	164	62	67	75	79	93	99
Si ₇ Au	5.50	5.55	4.24	4.36	123 (131 ^a)	132	93	59	32	52	103	84

^aThe corrected DFT value was used for potential fitting.

TABLE 5: Formation energy (eV) of substitutional and interstitial Au atoms in bulk Si compared to DFT values. The reference ground states for Si and Au are diamond and FCC, respectively. 64- and 216-atom systems are substitutional structures, and 65- and 217-atom systems are interstitial structures.

Point defects		DFT		MEAM
		64/65 atoms	216/217 atoms	
Substitutional Au		1.34 ^a	1.51 ^a , 1.62 ^b	1.55
Interstitial Au	Hexagonal	2.28 ^a	2.37 ^a , 2.61 ^b	2.331
	Tetrahedral	2.32 ^a	2.39 ^a , 2.60 ^b	2.332

^aCurrent work. ^b[31].

potential provides higher values of the structural energy differences in face-centered cubic (FCC)/body-centered cubic (BCC) and FCC/hexagonal close-packed (HCP) structures compared to the other calculation methods, suggesting that the current MEAM potential provides a more stable FCC structure.

Next, we performed density functional theory (DFT) calculations to obtain the necessary reference data for developing binary and ternary MEAM potentials. The exchange correlation functional is approximated by generalized gradient approximation (GGA) revised for solids by Perdew-Burke-Ernzerhof [26], with plane wave expansion up to the cutoff energy of 300 eV determined by convergence tests. The electronic structure as a function of the positions of atomic nuclei was tackled using the projector augmented wave method. The relaxation was repeated until the total energy reached below 10^{-5} eV and force below 0.01 eV/Å. The Brillouin zone was sampled with the Monkhost-Pack scheme. For calculating the cohesive energy, lattice constant, and elastic constants, $10 \times 10 \times 10$ k -points were used in the model with $1 \times 1 \times 1$ unit and $6 \times 6 \times 6$ k -points for point defects in $3 \times 3 \times 3$ units. The computations were completed using Vienna Ab initio Simulation Package (VASP) [27–29].

Some basic physical properties of Si and Au were calculated and compared with the experimental values (given in parentheses) to verify the reliability of the above simulation settings. The lattice constant of the Si crystal was 5.439 Å (5.431 Å), the cohesive energy 4.49 eV (4.63 eV), and the elastic constants C_{11} , C_{12} , and C_{44} were 157 GPa (166 GPa), 62 GPa (64 GPa), and 75 GPa (80 GPa), respectively. The calculated and experimental values for Au are listed in Table 2.

2.2. MEAM Potentials of Si-Au, Si-H, and H-Au Binary Systems

2.2.1. Si-Au Interaction. For the Si-Au binary system, it is necessary to precisely predict the lattice distortion and

changes in the elastic and energy properties of bulk Si when Au is introduced. The Si₇Au compound was modeled by replacing one Si atom in the cubic unit with an Au atom. This structure is considered for parameter tuning as it represents the bulk Si doped with a high Au concentration of 12.5%. Specifically, the lattice constant, cohesive energy, and elastic constants of Si₇Au and formation energies of the substitutional and interstitial Au in bulk Si were used in the parameterization. Owing to the absence of stable compound structures in the Si/Au phase diagram, b1-NaCl was chosen as the reference structure for the Si-Au binary system. Some other reference structures were considered but failed to yield predictions close to the reference values. As it is a hypothetical structure, the lattice constant and cohesive energy of b1-SiAu were adjusted slightly based on DFT data to obtain overall agreement with the reference data. Table 3 lists the MEAM parameters of the binary Si-Au system.

The performance of the potential for the Si-Au system was examined. First, the differences in the lattice constant, cohesive energy, and elastic constants between Si and Si₇Au were measured. The cohesive energy was calculated as

$$\frac{E_c}{(N_{\text{Si}} + N_{\text{Au}})} = \frac{(N_{\text{Si}}E_{\text{Si}} + N_{\text{Au}}E_{\text{Au}} - E_{\text{tot}})}{(N_{\text{Si}} + N_{\text{Au}})}, \quad (4)$$

where E_{Si} and E_{Au} are the free energies of Si and Au atoms, respectively, N_{Si} and N_{Au} are the numbers of Si and Au atoms in the compound, respectively, and E_{tot} is the total energy.

The results obtained from DFT and MEAM are compared in Table 4. When the concentration of Au is as high as 12.5%, the lattice distortion and energy shift can be accurately determined. The lattice constant of Si₇Au increased because of the repulsion between Si and Au atoms.

The elastic constants of Si₇Au, C_{11} , C_{12} , and C_{44} could not be predicted with equal accuracy, despite adjusting the parameter set or altering the reference structure, indicating the intrinsic limitation of the empirical model. Many studies have reported that the MEAM potential cannot well predict the elastic constants of alloys [14, 25, 30]. Therefore, C_{11} is usually emphasized when fitting the potential. The DFT value of 123 GPa was not directly used for parameterization owing to the nonignorable differences between the DFT-calculated and experimentally determined C_{11} values for Si. The MEAM potential for Si was fitted to the experimental elastic constants. Therefore, the correction (~ 8 GPa) to the DFT value is necessary. The error correction proposed by Ryu and Cai [25] averaged the differences between experimental and DFT results for pure Si and Au.

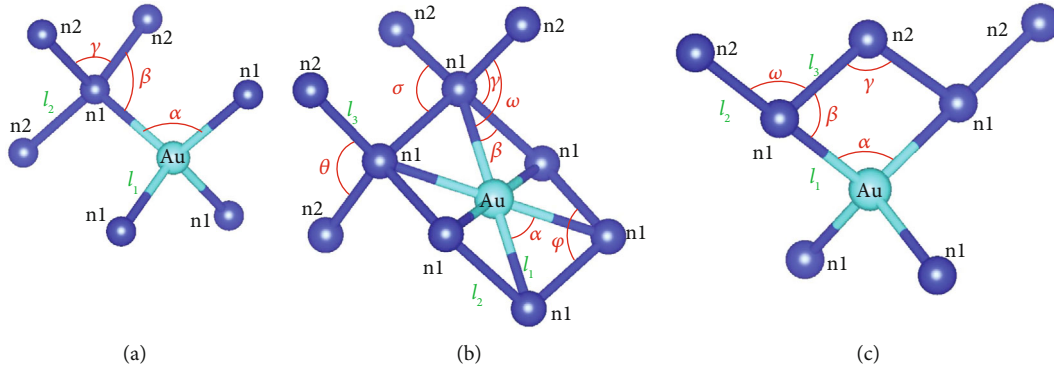


FIGURE 1: Labels used to characterize the lattice distortion induced by (a) substitutional, (b) hexagonal, and (c) tetrahedral Au.

TABLE 6: Geometrical information corresponding to Figure 1, with bond lengths in Å and angles in °. The bond length and angle are 2.35 Å and 109.47°, respectively, for pure Si.

Defect	Length/angle	DFT	MEAM
Substitution	l_1	2.43	2.47
	l_2	2.35	2.34
	α	109.48	109.47
	β	108.34	106.96
	γ	110.58	111.87
Hexagonal site	l_1	2.45	2.41
	l_2	2.55	2.53
	l_3	2.32	2.33
	α	62.70	63.37
	β	58.65	58.31
	γ	108.57	106.89
	ω	95.91	98.67
	θ	116.07	115.23
Tetrahedral site	l_1	2.50	2.47
	l_2	2.33	2.30
	l_3	2.44	2.45
	α	109.47	109.47
	β	68.23	69.89
	γ	114.08	110.75
	ω	111.78	108.83

Table 5 lists the formation energies of Au introduced in Si as a substitutional or interstitial atom. The MEAM predictions agreed well with DFT results, see Ref. [14] for energy calculation. Based on Dong's first principle study [31], a stable bridge interstitial site exists in addition to the hexagonal (Figure 1(b)) and tetrahedral (Figure 1(c)) sites. However, our DFT calculations showed that the bridge interstitial was metastable as the Au atom shifted to the tetrahedral site during relaxation. Therefore, it was not considered in the potential fitting.

An accurate description of the lattice distortion of the Au-doped Si crystal is required for a robust potential. The changes in the bond lengths and bond angles induced by the substitutional and interstitial Au atoms (Figure 1) were examined, where n1 and n2 represent the first and second nearest neighbor atoms. The results are listed in Table 6. The distortion can be quantified by comparing the calculated values with the bond length of 2.35 Å and bond angle of 109.47° in pure Si. The lattice distortion is mainly reflected by the change in bond length l_1 between Au and the first nearest neighbor Si. DFT and MEAM can predict the growth of l_1 , in accordance with the increased lattice constant of Si₇Au.

The MEAM potential can partially describe the surface reconstruction of SiNWs without H termination. The (2 × 1) reconstruction on the (1 0 0) facets can be reproduced, as shown in Figures 2(a) and 2(c). However, the MEAM model cannot correctly describe the undulating surface reconstruction on the (1 1 0) facets, see the comparison between Figures 2(b) and 2(c). This unique reconstruction stems from the semiconducting nature of this material. Incorrect descriptions may lead to unpredictable deviations in the simulation results. Nevertheless, some other important surface properties can be reproduced using the MEAM potential. For example, the outermost surface shrinks toward the subsurface, as observed in another study [16].

To eliminate the disparity in surface reconstruction, the dangling bonds were saturated with H. Figures 2(e) and 2(f) and demonstrate the same surface reconstruction pattern, indicating the necessity of H termination for this study.

2.2.2. Si-H Interaction. Our simulations only require H-covered SiNWs, while the interactions between H and bulk Si with interstitial H or H₂ were not considered. Therefore, the MEAM parameter optimization of the Si-H binary system focused on the structural and vibrational properties of the Si-H compounds and H-covered Si surfaces. Table 3 lists the MEAM parameters of the Si-H binary system. Notably, diamond was selected as the reference structure to obtain better thermal stability and vibrational characteristics.

Table 7 lists the structural parameters of the Si-H molecules predicted by MEAM, including the bond length, bond angle, and vibrational wave number. The Si-H bond energies

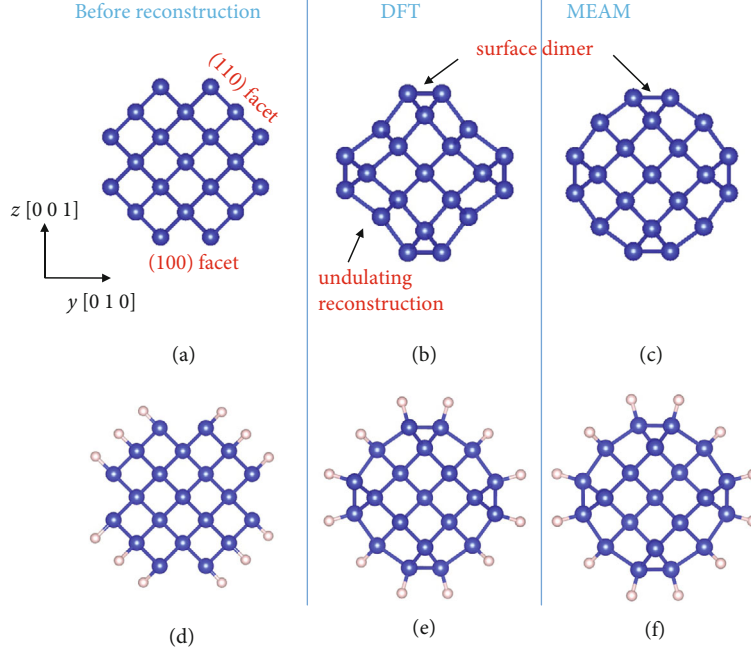


FIGURE 2: Unrelaxed cross-section of the ultrathin $[1\ 0\ 0]$ SiNW (a) before and (d) after H termination. (b) Undulating reconstruction on $(1\ 1\ 0)$ facets and (2×1) reconstruction on $(1\ 0\ 0)$ facets predicted by DFT calculations, while (c) the MEAM potential can only predict (2×1) reconstruction. (e) and (f) Comparison of the reconstructions showing that H termination can eliminate the disparity in description on reconstruction.

in the molecules were not calculated because the reference structure of the Si-H binary system was not a dimer. Within the framework of the MEAM model, the bond energy was obtained based on the reference structure of diamond, which deviated significantly from the value obtained using dimeric SiH as the reference structure. The bond energy of dimer-Si₂ predicted by MEAM was 3.87 eV, which differed significantly from the theoretical value of 3.13 eV [32]. In this circumstance, we turned the description of energy to the vibrational wave number as it measures the change of energy as a function of the bond length. Furthermore, the vibrational wave numbers predicted by MEAM agree well with the reference values. In structural properties, the MEAM estimations also agree well with the reference values, except for the bond angles $\theta_{\text{H-Si-Si}}$ in Si₂H₄, $\theta_{\text{H-Si-H}}$ in SiH₂, and $\theta_{\text{H-Si-Si}}$ in SiH₃SiH, probably owing to the inadequate description of the π -bonding.

Regarding the SiNWs, the properties of H-covered surfaces are important. Therefore, the energy as well as the structural and vibrational properties of the H-terminated surfaces of c-Si were investigated for verification.

The reconstruction pattern of the $(1\ 0\ 0)$ surface mainly depends on the H coverage. Figure 3(a)–3(c) illustrate the (2×1) monohydride, (3×1) alternate monohydride/dihydride, and (1×1) dihydride structures produced by the MEAM potential, in line with experimental observations. As for the structural details, the Si-Si bond length on the surface of the (2×1) structure was 2.44 Å, consistent with the value of 2.4 Å [33] obtained by first-principle calculations. In addition, the bond angle of H-Si-Si 112° agrees well with other predictions 112.4° [32] and 114.7° [34]. In the (3×1) structure, the Si-Si bond length in the (2×1) part was

2.97 Å, significantly higher than the first principle prediction 2.41 Å [33]. The bond angle of H-Si-H in the (1×1) part was 112°, closed to the first principle prediction 109° [33]. In the (1×1) structure, the H-Si-H bond angle was 108°, larger than the first principle prediction 102°. Contrary to experimental observations, the asymmetric (1×1) reconstruction shown in Figure 3(c) is more stable than its symmetric counterpart, albeit close in energy [35]. In conclusion, the optimized MEAM potential provides a more accurate description of the (2×1) reconstruction. Therefore, the $(1\ 0\ 0)$ facets of the specimens tested in the next section were modeled in the (2×1) reconstruction.

The wave number of the stretch mode of $(1\ 0\ 0)$ monohydride is 2099 cm⁻¹, measured experimentally [36], and the (1×1) H coverage on the $(1\ 1\ 1)$ surface gives a stretch mode wave number 2084 cm⁻¹. The corresponding MEAM predictions of 2191 cm⁻¹ and 2068 cm⁻¹ agree well with the experimental values.

The formation energies of H covering on the Si surfaces were considered in the parameterization, defined as follows:

$$E_f = \frac{(E_{\text{tot}} - n_{\text{Si}}E_{\text{Si}} - n_{\text{H}}E_{\text{H}})}{n_{\text{bond}}}, \quad (5)$$

where E_{tot} is the total energy of the Si surface terminated by H, E_{Si} and E_{H} are the atomic average energy under the ground state, n_{Si} and n_{H} are the numbers of Si and H atoms in the system, and n_{bond} is the number of Si-H bonds. The model used for calculation had a surface with 2×2 units and 3 crystalline units in thickness. Table 8 compares the formation energies calculated using MEAM and DFT.

TABLE 7: Comparison of the structural information (bond length in Å, angle in °) and vibrational wave number (cm^{-1}) for Si-H molecules, predicted by MEAM, experimental and theoretical methods, and other empirical calculations.

	Property	Expt./theory	Tersoff [32]	MEAM
H ₂	$l_{\text{H-H}}$	0.74 ^a	0.74	0.74
	ν	4400 ^a	4400	4376
SiH ₄	$l_{\text{Si-H}}$	1.48 ^a	1.475	1.49
	$\theta_{\text{H-Si-H}}$	109.5 ^a	109.5	109.5
	ν	2186 ^a	2100	2094
Si ₂ H ₆	$l_{\text{Si-H}}$	1.49 ^a , 1.50 ^b	1.48	1.50
	$l_{\text{Si-Si}}$	2.40 ^a , 2.33 ^b	2.33	2.35
	$\theta_{\text{H-Si-Si}}$	110.3 ^a , 110.1 ^b	109.4	108.2
	ν	2155 ^a	2150	2108
Si ₂ H ₄	$l_{\text{Si-H}}$	1.48 ^a , 1.50 ^b	1.48	1.52
	$l_{\text{Si-Si}}$	2.33 ^a , 2.31 ^b	2.40	2.32
	$\theta_{\text{H-Si-H}}$	112.8 ^a , 114.3 ^b	106.0	108.7
	$\theta_{\text{H-Si-Si}}$	118.9 ^a , 120.1 ^b	106.0	109.3
	ν	—	—	2102
SiH	$l_{\text{Si-H}}$	1.51 ^a , 1.55 ^b	1.51	1.56
	ν	2042 ^a	2034	2145
SiH ₂	$l_{\text{Si-H}}$	1.51 ^a , 1.54 ^b	1.51	1.52
	$\theta_{\text{H-Si-H}}$	92.1 ^a , 89.8 ^b	92.3	110.3
	ν	2032 ^a	2136	2122
SiH ₃	$l_{\text{Si-H}}$	1.48 ^a , 1.50 ^b	1.48	1.50
	$\theta_{\text{H-Si-H}}$	110.5 ^a , 110.7 ^b	106.0	110.1
	ν	1955 ^a	2051	2078
SiH ₃ SiH	$l_{\text{Si-Si}}$	2.39 ^a , 2.38 ^b	2.37	2.28
	$l_{\text{Si-H}} (1^\circ)$	1.48 ^a , 1.51 ^b	1.48	1.50
	$l_{\text{Si-H}} (2^\circ)$	1.51 ^a , 1.54 ^b	1.51	1.55
	$\theta_{\text{H-Si-Si}} (1)$	114.2 ^a , 114.0 ^b	109.5	108.8
	$\theta_{\text{H-Si-Si}} (2)$	89.1 ^a , 93.1 ^b	92.3	109.2

^aData calculated in [32] or quoted therein. ^bPresent DFT calculations. ^c1 and 2 represent the SiH₃ and SiH clusters, respectively.

2.2.3. *H-Au Interaction.* Au atoms are located within the SiNWs, and they have no complicated interactions with H atoms. Therefore, the parameterization of the H-Au binary system was conducted considering only the relationship between the potential energy of a dimeric AuH system and the atomic distance. The optimized parameters are listed in Table 3, and the corresponding potential-distance curve is plotted in Figure 4. Within the range 0.45~3.7 Å, the potential energy is perfectly reproduced by MEAM.

2.3. *Si-H-Au Interaction.* During the dynamic vibrations of SiNWs, the interactions of the H atoms with the Au-doped NWs are not complex because the H atoms are located outside the surface. The diffusion of H atoms into the NWs is beyond the scope of this study. However, when the Au

atoms approach the surface, particularly in the cutoff distance from the H atoms, the force field of the ternary system works. The six parameters required to obtain the final MEAM potential of the Si-H-Au ternary system are listed in Table 9. They characterize the degree of screening of the interactions between the third element and the adjacent two elements. The values were calculated using Jang's method [30], based on the premise that the degree of screening by atom Y (in X-Y-Z) to the interaction between atoms X and Z is the average between those to the X-X and Z-Z interactions.

To verify the reliability of the parameter set, the formation energies of a substitutional Au atom located at the sub-surface of the H-covered surface were calculated and compared with those obtained using DFT, see Table 10. Although the MEAM parameters were not optimized targeting the DFT values, the MEAM predicted values agreed well with the reference values. Au located at the outermost surface was not considered because a previous DFT study [37] showed that the local reconstruction caused by Au was rather complex, which is beyond the description of MEAM.

3. Vibrational Properties of H-Covered SiNWs Doped with Au

3.1. *Modeling and Vibrational Test.* After consulting relevant literature, we can only determine the cross-sectional shape of [1 0 0] and [1 1 0] SiNWs. The cross-section of the ultrathin [1 0 0] SiNW is octagonal with four (1 0 0) facets and four (1 1 0) facets [38], as shown in Figure 5(b). The (1 0 0) facets are in the (2 × 1) reconstruction. The cross-section of the ultrathin [1 1 0] SiNW is hexagonal with two (1 0 0) facets and four (1 1 1) facets [38], see Figure 5(c). Au atoms randomly replace Si atoms according to the doping concentration. Other forms of doping were not considered owing to the absence of the doping profile of Si-Au compounds. According to Liang's first principle study, Au is likely to be located at the substitutional sites [39]. As Au and Si are not congeners in the same group, when Au is located on the surface of the NWs, it would generate complex surface reconstructions that cannot be described using the MEAM potential. Therefore, the doping region is enclosed within the subsurface. Actually first-principles calculations [39, 40] and experiments [41] suggested that the core region of SiNWs is energetically favorable for Au atoms.

The model size was determined according to the available computing resources. Because of the complexity of the MEAM scheme and the large cutoff distance (6 Å), it is considerably more expensive than SW, Tersoff, and EAM models. Besides, the investigation on the influence of Au on the quality factor of SiNWs requires at least 5 ns. To address the above concerns, the [1 0 0]-SiNW for vibrational tests was 3.3 nm in diameter and 18.5 nm in length, containing 9282 atoms (1496 H atoms); the [1 1 0]-SiNW was 3.4 nm in diameter and 13.8 nm in length, containing 7200 atoms (1152 H atoms). To compare the vibrational characteristics of the H-covered and bare NWs, the bare [1 0 0]-SiNWs were obtained by removing the H atoms of the H-covered specimens. Another reason for not preparing larger

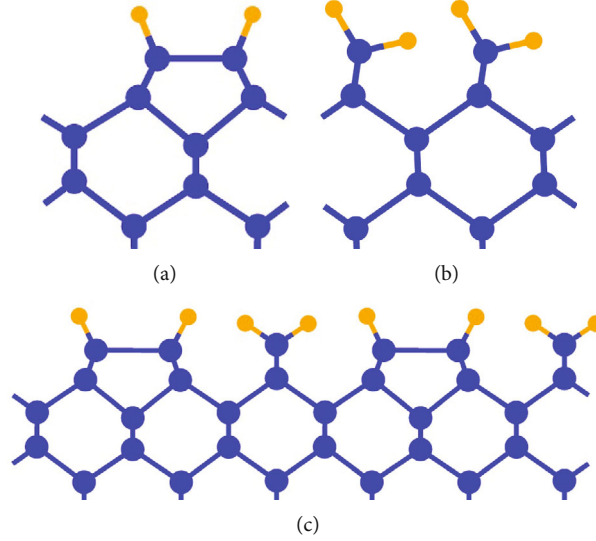


FIGURE 3: MEAM predicted reconstructions of the (1 0 0) surface with different H coverage. (a) (2×1) monohydride. (b) Alternate (3×1) monohydride/dihydride. (c) Asymmetric (1×1) dihydride.

TABLE 8: Formation energy (eV) of H termination on Si surface.

H covered surface	Surface energy	
	DFT	MEAM
(1 0 0)- (2×1) reconstruction	0.19	0.11
(1 1 0)-monohydride	0.30	0.27
(1 1 1)-monohydride	0.29	0.25

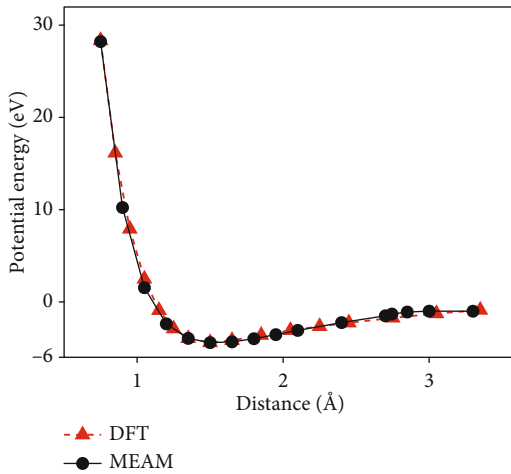


FIGURE 4: Potential energy as a function of atomic distance, calculated using the MEAM potential and DFT.

specimens is that the size effects on the vibrational characteristics have already been studied [12].

The SiNW was first relaxed to a minimum energy state using the conjugate gradient method. Then, the SiNW was equilibrated at 10 K using Nose-Hoover thermostat (NVT ensemble) for 100 ps so that the NW could further release the residual stress and reach thermodynamic equilibrium. After static and dynamic relaxations, one lattice unit at both ends of the SiNW was fixed, and a sinusoidal velocity field

$v(x) = a \sin(kx)$ ($0 \leq x \leq L$) was applied to the movable part, as shown in Figure 5(a). The amplitude a was 0.8 \AA/ps , small enough to prevent nonlinear vibration. In the last step, the SiNW vibrated under the constant energy ensemble (NVE) for 5 ~ 10 ns. The length of time t depended on the period of beat phenomenon, T_b . If T_b was higher than t , then the vibration continued and exceeded one beat period. The coordinates of the center of mass (COM) and energy during vibration were recorded. The computations were accomplished through the large-scale atomic/molecular massively parallel simulator (LAMMPS) [42], using 2 nodes with 16 cores. Each test took 7 ~ 15 hours, depending on the time span of the vibration.

3.2. Natural Frequency Decrease Caused by the Impurity Au. Fast Fourier transform (FFT) was applied to the time history of the potential energy or root mean square (RMS) of the COM to obtain the first-order natural frequency. The RMS of the COM was considered for later analysis of Q . We considered a [1 0 0] sample in the 3% group as an example to illustrate signal processing. Figure 6(a) plots the time history of the potential energy and the magnified view of the periodic vibration. The period is constant although the oscillation amplitude keeps changing. FFT provides one-sided power spectra, as shown in Figure 6(c). Although the FFT magnitude is different between these two signals, the spectrum distribution is consistent, as the two peaks in each curve correspond to the same frequencies. This indicates that the RMS of the COM can replace the energy for frequency analysis.

The effect of Au on the resonant frequency was investigated considering two aspects, concentration and distribution. To this end, five samples with different impurity distribution were prepared for each concentration ($\leq 7\%$). The natural frequency as a function of concentration is plotted in Figure 7, which exhibits an evident linear downward trend from 0 to 7%. The error bar corresponding to each

TABLE 9: Parameters for the Si-H-Au ternary system.

Parameter	Value	Calculation formula
C_{\min} (Si-H-Au)	2.10	$[0.5C_{\min}(\text{Si-H-Si})^{1/2} + 0.5C_{\min}(\text{Au-H-Au})^{1/2}]^2$
C_{\min} (Si-Au-H)	2.00	$[0.5C_{\min}(\text{Si-Si-H})^{1/2} + 0.5C_{\min}(\text{Au-Au-H})^{1/2}]^2$
C_{\min} (H-Si-Au)	2.00	$[0.5C_{\min}(\text{H-H-Au})^{1/2} + 0.5C_{\min}(\text{Si-Si-Au})^{1/2}]^2$
C_{\max} (Si-H-Au)	3.14	$[0.5C_{\max}(\text{Si-H-Si})^{1/2} + 0.5C_{\max}(\text{Au-H-Au})^{1/2}]^2$
C_{\max} (Si-Au-H)	3.28	$[0.5C_{\max}(\text{Si-Si-H})^{1/2} + 0.5C_{\max}(\text{Au-Au-H})^{1/2}]^2$
C_{\max} (H-Si-Au)	2.80	$[0.5C_{\max}(\text{H-H-Au})^{1/2} + 0.5C_{\max}(\text{Si-Si-Au})^{1/2}]^2$

TABLE 10: Formation energies (eV) of Au located at the subsurface of the Si surfaces with H termination. The models considered here are the same as those in Table 8.

Subsurface	Formation energy	
	DFT	MEAM
(1 0 0)-(2 × 1) reconstruction	1.26	1.43
(1 1 0)-Monohydride	1.55	1.54
(1 1 1)-Monohydride	1.39	1.51

concentration is negligible compared to the frequency value, indicating that the impurity distribution has a negligible influence on the natural frequency.

The two adjacent peaks in the spectrum indicate the vibrations in two orthogonal directions [43], as plotted in Figure 6(c), which are denoted as the elementary directions. Synthesizing the two vibrations results in the beat phenomenon [44]. Symmetry breaking in NWs leads to the deflection of the elementary directions [13]. Obviously, Au doping caused lattice asymmetry owing to the significant difference in the atomic masses of Au and Si, theoretically leading to the deflection of the elementary directions. However, the simulation results for [1 1 0] SiNWs showed that the elementary directions remained unchanged (i.e., the y and z orientations in Figure 5(c)) or deflect at a negligible angle, irrespective of different doping concentrations, distributions, or initial excitation directions. These aspects will be further explained in the next part, with this part focusing on the frequency. The frequencies along the elementary directions depend on the symmetry. The frequencies along the elementary directions y and z in the [1 0 0] SiNWs are close (see Figure 6(c)) even though the elementary axes deflect significantly, whereas those in the [1 1 0] SiNWs differ considerably. Therefore, only the values of the principal peaks in the FFT curve of the [1 0 0] SiNWs are plotted in Figure 7.

The effects of H termination on the frequency were investigated. The trend for bare [1 0 0] samples is linear, similar to the H-covered counterparts, as shown in Figure 7. H termination causes a slight decrement in frequency but does not affect the gradient. These results suggest the advantages of MD simulations involving the NWs with complex cross-sections over theoretical calculations. Based on the Euler-Bernoulli beam theory (EBBT), He and Lilley [10] developed a new formula to calculate the natural fre-

quency of a double-clamped beam considering surface stress, i.e., $f_0 = f_n \sqrt{0.025\eta + 1}$ and $\eta = 2\tau DL^2/(EI)^*$. f_n , τ , D , L , and $(EI)^*$ are the frequency obtained using EBBT, surface stress, diameter, length, and effective bending moment, respectively. The equation is unsuitable for the H-covered SiNWs, because of not only the simplification of the formula itself but also the approximation of the diameter, effective bending inertia, and surface stress that makes it difficult to capture the small differences accurately.

3.3. Beat Phenomenon. The beat phenomenon stems from the superposition of two harmonic vibrations with close frequencies. For the convenience of theoretical analysis, the amplitude attenuation was ignored. For two harmonic vibrations described by $U_i = A_i \sin(\omega_i t)$, $D_i = A_i \sin(\omega_i t)$, where $\omega_i = 2\pi f_i$, $i = y, z$, the total external energy of the NW with mass M can be expressed as [13]

$$\begin{aligned}
 E_e &= \sum_{i=1,2} \frac{1}{2} M A_i^2 \omega_i^2 \sin^2(\omega_i t) = A_{\text{etot}} - A_{\text{etot}} \cos[(\omega_1 - \omega_2)t] \\
 &\quad \cdot \cos[(\omega_1 + \omega_2)t] + (M A_1^2 \omega_1^2 - M A_2^2 \omega_2^2) \\
 &\quad \cdot \sin[(\omega_1 - \omega_2)t] \sin[(\omega_1 + \omega_2)t] \\
 &\approx A_{\text{etot}} - A_{\text{etot}} \cos[(\omega_1 - \omega_2)t] \cos[(\omega_1 + \omega_2)t],
 \end{aligned} \tag{6}$$

where $A_{\text{etot}} = (M A_1^2 \omega_1^2 + M A_2^2 \omega_2^2)/4$ is the amplitude of the total external energy. The approximation in Equation (6) is based on the premise $\omega_y \approx \omega_z$ and $\sin[(\omega_y - \omega_z)t]$ approaching 0. Equation (6) presents a vibration with the oscillating amplitude at a low frequency, following $A_{\text{etot}} \cos[(\omega_y - \omega_z)t]$.

The vibration decomposes into two elementary directions when the initial stimulus is along an arbitrary direction in the cross-section, resulting in a beat phenomenon [13]. Different impurity distributions create different symmetries determined by the mass distribution rather than the geometry. In this way, the elementary coordinate system changes with the distribution. Therefore, different distributions can lead to different beat phenomena because the elementary directions change. However, the theoretical possibility explained above is inconsistent with the simulation results for [1 1 0] SiNWs, the elementary directions of which remained unchanged or deflected at negligible

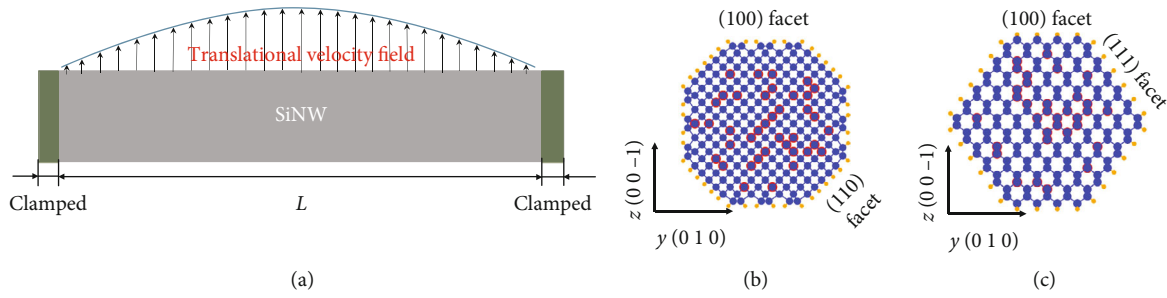


FIGURE 5: (a) Schematic of a clamped-clamped SiNW used for vibrational tests. A sinusoidal velocity field introduces the initial excitation. (b) Cross-section of the $[1\ 0\ 0]$ SiNW. (c) Cross-section of the $[1\ 1\ 0]$ SiNW. Si, Au, and H atoms are colored blue, orange, and yellow, respectively.

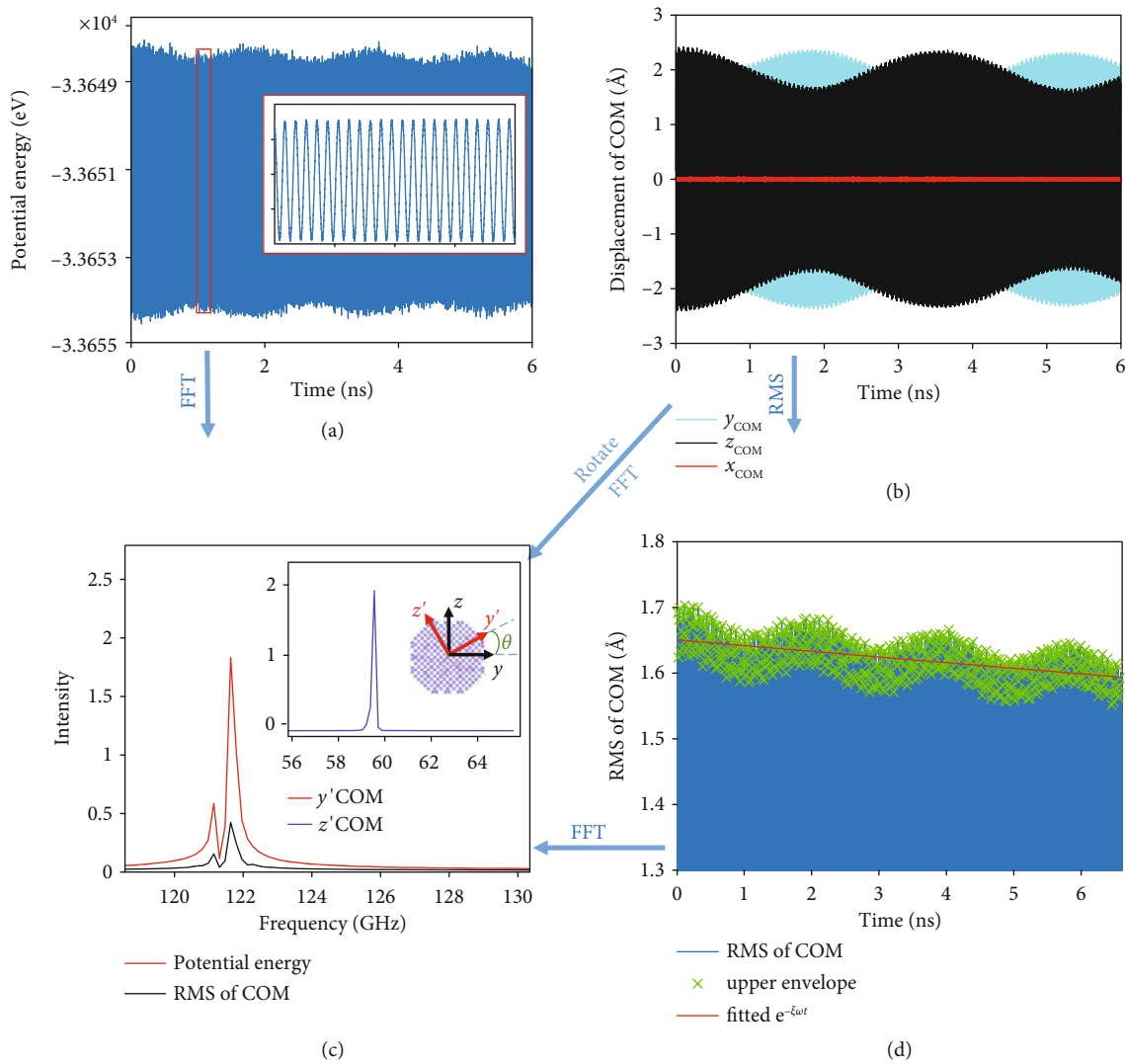


FIGURE 6: Processing of the vibrational information. A $[1\ 0\ 0]$ sample in the 3% group was taken as an example. It was initially excited by the stimuli along y and z as a superposition. Time histories of (a) potential energy, (b) y_{COM} and z_{COM} , and (d) RMS of COM exhibit beat phenomena, reflected by the two adjacent peaks in the spectrum distribution obtained by FFT (c). The inset gives the FFT spectrum of the new elementary directions y' and z' , along which the beat phenomena disappear. (d) Attenuation of the upper envelope corresponding to the dissipation of mechanical energy.

angles. It is interesting to examine the robustness of the elementary directions. According to the model pattern used in this work, several possible factors could cause

the deflection of the elementary directions, including H termination, and the impurity concentration and distribution.

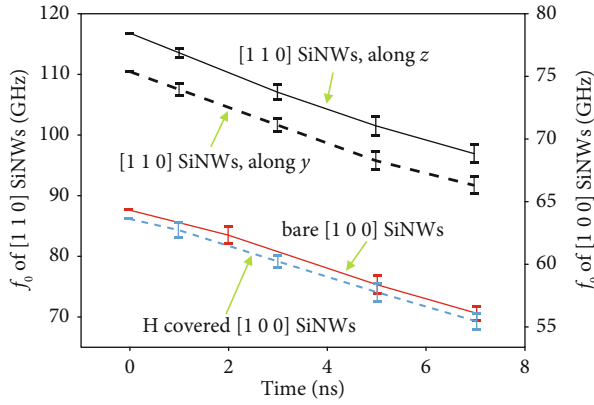


FIGURE 7: Resonant frequency of the double-clamped SiNWs as a function of doping concentration. The error bar corresponding to each concentration was sampled from five specimens with different impurity distributions.

First, the effects of H termination were investigated. One (Figure 8(a)) of the five [1 1 0] samples in the 7% group was tested after removing the H atoms. The stimulus direction was anticlockwise at $\pi/4$ from y . The time history of the COM along z and the corresponding FFT is shown in Figure 8(b). The beat phenomenon can be observed, which is characterized by the auxiliary peak, suggesting the deflection of the elementary directions. The new elementary coordinate system $y'-z'$ could be obtained using the following transformation matrix:

$$\begin{bmatrix} y' \\ z' \end{bmatrix} = \begin{bmatrix} \cos \theta & -\sin \theta \\ \sin \theta & \cos \theta \end{bmatrix} \begin{bmatrix} y \\ z \end{bmatrix}, \quad (7)$$

where θ is the deflection angle between $y'-z'$ and $y-z$, and it was obtained by trial and error until no beat phenomenon appeared along y' and z' . θ was 0.0095π in this case, obviously a negligible angle. The vibration in the transformed coordinate system is shown in Figure 8(c), without the beat phenomenon. It is worth mentioning that the H-covered counterpart of this model showed no beat phenomenon, indicating that H coverage can improve the robustness of the elementary directions to a certain extent.

Although the elementary directions proved robust against the impurity concentration and distribution, different beat periods for the five samples in each group with different concentrations were obtained. This is because once the elementary direction changes, the frequency along this direction changes accordingly. The beat angular frequency is $(\omega_y - \omega_z)$. A slight change in ω_y or ω_z would result in a different beat frequency.

The beat frequency can be calculated as follows considering an NW with a fixed cross-section and length [43].

$$\omega_y - \omega_z \propto \left| \sqrt{I_y} - \sqrt{I_z} \right|, \quad (8)$$

where I is the moment of inertia. However, this equation could not be used to estimate the beat frequency due to the

randomness in the distribution of Au atoms. Therefore, symmetry breaking is difficult to quantify. Hence, this study applied an alternative method to characterize the degree of symmetry breaking, i.e., the enveloping cylindrical surface (sharing the same axis with the NW) of the axial mass distribution curve. The radius of the enveloping cylindrical surface in the bare NW (Figure 8(a)) is 1.95 \AA and 1.93 \AA for the H-covered counterpart. The slightly lower value indicates better symmetry.

Then, the effects of the symmetry of the mass distribution were investigated, considering more extreme situations, i.e., when the impurity atoms were radially and axially segregated. Figure 8(d) presents a SiNW with Au segregated in half of the region, which was constructed based on the H-covered counterpart in Figure 8(a) obtained by replacing the Au atoms in the other half region with Si atoms. The radius of the enveloping cylindrical surface increased to 2.34 \AA , indicating deteriorated symmetry. The excitation direction was the same as above. As observed in Figure 8(e), the model shows a slight beat phenomenon. The auxiliary peak rotates $y-z$ by 0.0064π to obtain the new elementary coordinate system $y'-z'$. The transformed vibrational signal and spectrum are plotted in Figure 8(f). The rotation angle is also negligible, indicating that radial symmetry breaking slightly affects the deflection of the elementary directions. In comparison, axial symmetry breaking will not cause the deflection of the elementary directions. The model shown in Figure 8(g) is the H-covered counterpart of Figure 9(a) with only one-third of the doped region in the axial direction. The result (Figure 8(h)) shows no beat phenomenon, suggesting that the elementary directions remain unchanged.

The above investigations lead to the conclusion that the robustness of the elementary directions in the [1 1 0] SiNWs is hardly affected by impurity Au atoms. However, from a rigorous point of view, the robustness may also be related to the cross-section pattern and boundary conditions (e.g., clamped on one side) or other factors associated with impurity Au atoms, which is a topic for future work. Furthermore, the reason that [1 0 0] SiNWs do not possess this characteristic is also an interesting topic. Actually, for most Au-doped [1 0 0] samples, we failed to find the new elementary axes $y'-z'$ using Equation (7), irrespective of how we adjust θ , and the FFT curves for y' and z' always exhibited an auxiliary peak. Thus, we can preliminarily infer that this behavior is closely related to the symmetry difference and the original elementary directions.

This section explains that the unintentional impurity Au atoms will not cause serious deflection of the elementary axes in the [1 1 0] SiNWs. When applied in ultrasensitive resonators, the symmetry breaking induced by the impurity distribution will not produce a large frequency shift. It will not cause disturbance during signal testing. According to the advanced mass detection technique developed by Gil Santos et al. [45], the position and mass of the adsorbate can be obtained by the relative shift of frequencies in two orthogonal directions. Effective restraints on extra frequency shifts caused by the deflection of elementary directions are required. [1 1 0] SiNWs can meet this need because their elementary axes are robust.

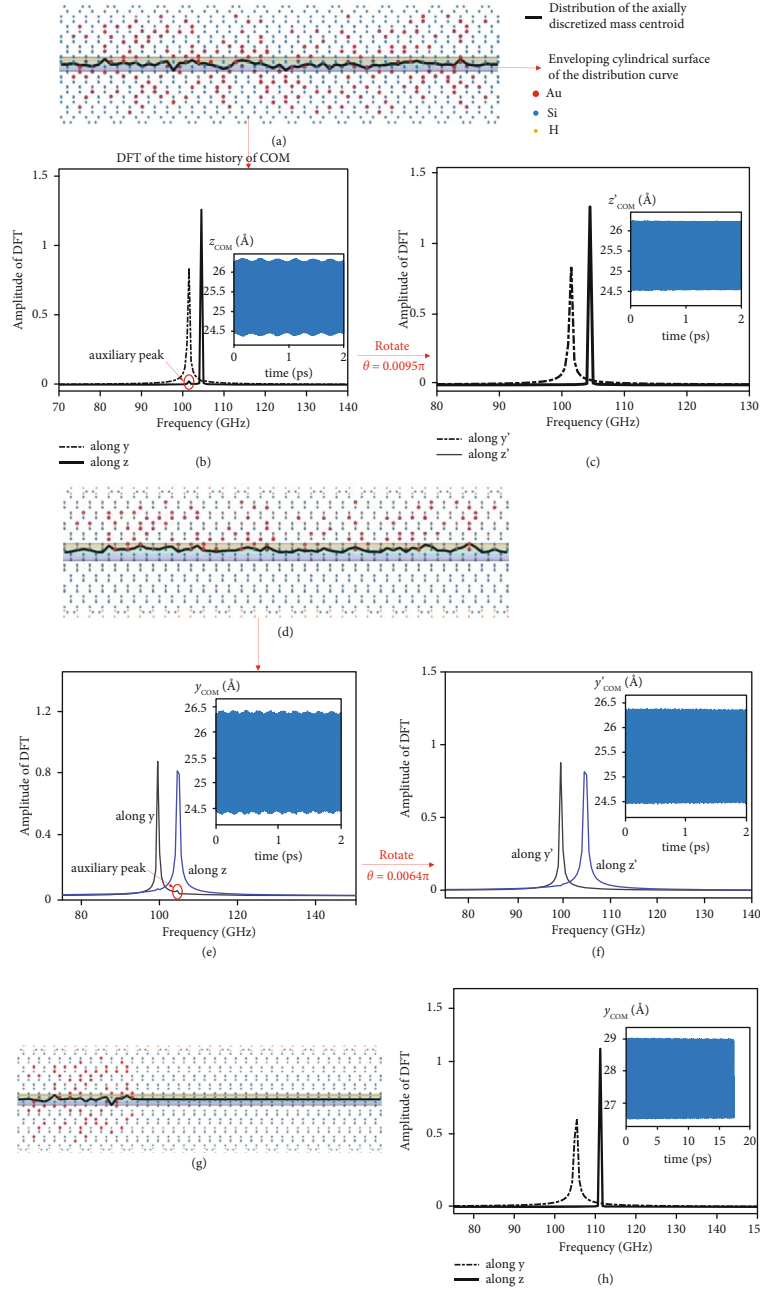


FIGURE 8: Effects of H termination (a)~(c), radial (d)~(f), and axial impurity segregation (g, f) on the deflection of the elementary directions. (b) Appearance of the beat phenomenon after removing the H atoms on the surface of a sample in the 7% group (a) and disappearance after rotating the coordinate system by 0.0095π (c). Deteriorated radial symmetry (d) resulting in the beat phenomenon (e) and its disappearance after rotating the coordinate system by 0.0064π (f). Axial symmetry breaking (g) causing no deflection of the elementary directions (h).

3.4. Quality Factor Q . Q quantifies the energy dissipation rate of a resonator, defined as the ratio between the total external energy and the average energy loss in one cycle at the resonant frequency. MD can output the total energy, including the external energy (or mechanical energy) and internal energy (or thermal energy). It is inconvenient to extract the external energy to obtain Q ; thus, we used an alternative method, i.e., the RMS of the COM [46]. The amplitude of the RMS decreases following the exponential law $Ae^{-\xi\omega t}$, where ξ is the damping ratio, and $\omega = 2\pi f_0$ is the

angular frequency, with f_0 obtained from FFT. Moreover, Q is equal to $1/2\xi$.

The Q values for $[1\ 0\ 0]$ and $[1\ 1\ 0]$ SiNWs are plotted in Figure 9(a) as a function of concentration. The graph shows an overall downward trend, accompanied by the enlarged error bar. Besides, the impurity distribution considerably magnifies the scattering of Q . The scattering of Q is amplified as the concentration increases. In this case, we cannot safely capture the varying trend of Q as a function of the concentration due to the small sample size. In addition to

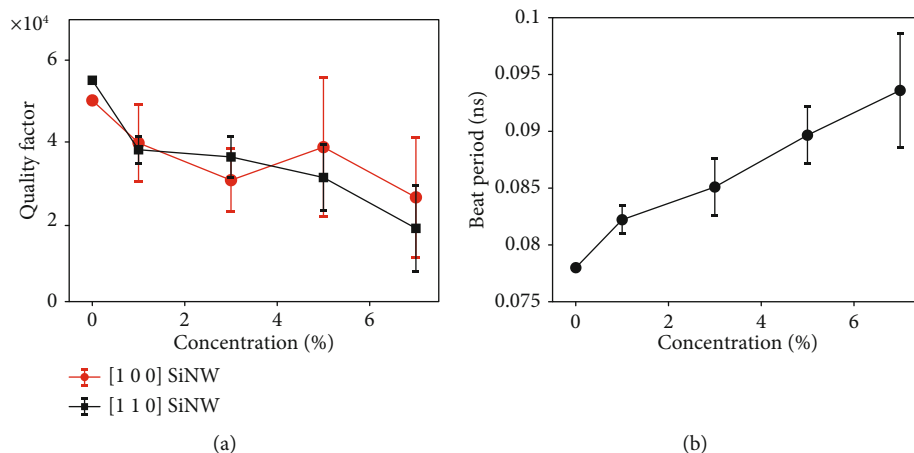


FIGURE 9: (a) Quality factor of [1 0 0] and [1 1 0] and (b) beat period T_b SiNWs as a function of concentration.

external damping, atomic friction is also an important factor for energy dissipation [47]. According to Islam et al. [4], impurity atoms can promote friction, which results in decreased Q . Therefore, the downward trend is logically correct.

The strong dependence of the beat period, $T_b = 2\pi/(\omega_y - \omega_z)$, of the [1 1 0] SiNWs on the concentration is shown in Figure 9(b). The longer the beat period, the larger is the deflection of the elementary coordinate system. Although the elementary coordinate system is robust, a slight deflection can lead to an obvious beat phenomenon. From Figures 9(a) and 9(b), one can infer that the deflection of the elementary axes accelerates the vibrational energy dissipation. This feature was not observed in the [1 0 0] SiNWs, probably because of the same geometric symmetry along y and z .

More computational resources are required to reveal the relationship between Q and the doping concentration than for the other properties, only to obtain the downward trend and increased scattering. Nevertheless, these findings have engineering significance. For example, high Au concentrations should be avoided for standardizing SiNW-based resonators.

4. Conclusion

MD was applied to investigate the influences of Au, a commonly used catalytic metal, on the vibrational characteristics of SiNWs, using a newly developed MEAM potential for the Si-H-Au ternary system. The parameterization targets the fundamental properties of H-covered SiNWs with impurity Au, mainly including Au-induced changes in the structure, energy, and elasticity of bulk Si and the properties of H-terminated Si surfaces. Au doping causes evident changes in resonant frequency f_0 and quality factor Q . Both these parameters decrease with the concentration; the former drops linearly, whereas the latter just shows a downward trend accompanied by the amplified error bar. This indicates that Q is sensitive to the distribution of impurities while f_0 is not. Besides, the deflection of the elementary axes leads to a

higher energy dissipation rate. An interesting observation is that the elementary coordinate system of [1 1 0] SiNWs remains stable. The deflection angle is rather small, even when the impurities are segregated. This observation suggests that when used as ultrasensitive resonators, [1 1 0] SiNWs can effectively restrain the unwanted frequency shift potentially caused by the impurity induced deflection of the elementary axes.

Data Availability

All data, models, and code for model construction are available from the corresponding author by request.

Conflicts of Interest

The authors declare no conflict of interest.

Acknowledgments

This work is financially supported by the National Natural Science Foundation of China (No. 51705522, No. 51705526) and the Youth Program of Xi'an Research Institute of Hi-Tech (No. 01122202).

References

- [1] A. Koumela, D. Mercier, V. Gouttenoire, C. Marcoux, S. T. Purcell, and L. Duraffourg, "Silicon nanowire resonator with integrated electrostatic actuation," *Procedia Engineering*, vol. 25, pp. 1649–1652, 2011.
- [2] E. Mile, G. Jourdan, I. Bargatin et al., "In-plane nanoelectromechanical resonators based on silicon nanowire piezoresistive detection," *Nanotechnology*, vol. 21, no. 16, article 165504, 2010.
- [3] S. Zhao, Y. Shen, A. Li, Y. Chen, and D. Wei, "Effects of rare earth elements doping on gas sensing properties of ZnO nanowires," *Ceramics International*, vol. 47, no. 17, pp. 24218–24226, 2021.
- [4] M. Islam, M. S. H. Thakur, S. Mojumder, A. A. Amin, and M. M. Islam, "Mechanical and vibrational characteristics of functionally graded cu-Ni nanowire: a molecular dynamics

- study," *Composites Part B Engineering*, vol. 198, article 108212, 2020.
- [5] D. Georgakaki, O. G. Ziogos, and H. M. Polatoglou, "Vibrational and mechanical properties of Si/Ge nanowires as resonators: A molecular dynamics study," *physica status solidi (a)*, vol. 211, no. 2, pp. 267–276, 2014.
 - [6] S. Ryu and W. Cai, "Molecular dynamics simulations of gold-catalyzed growth of silicon bulk crystals and nanowires," *Journal of Materials Research*, vol. 26, no. 17, pp. 2199–2206, 2011.
 - [7] W. Chen, L. Yu, S. Misra, Z. Fan, and P. R. I. Cabarrocas, "Incorporation and redistribution of impurities into silicon nanowires during metal-particle-assisted growth," *Nature Communications*, vol. 5, no. 1, p. 4134, 2014.
 - [8] M. Sansa, M. Fernandez-Regulez, A. S. Paulo, and F. Perez-Murano, "Electrical transduction in nanomechanical resonators based on doubly clamped bottom-up silicon nanowires," *Applied Physics Letters*, vol. 101, pp. 061101–062689, 2012.
 - [9] J. M. Nichol, E. R. Hemesath, L. J. Lauhon, and R. Budakian, "Controlling the nonlinearity of silicon nanowire resonators using active feedback," *Applied Physics Letters*, vol. 95, no. 12, pp. 123116–123597, 2009.
 - [10] J. He and C. M. Lilley, "Surface stress effect on bending resonance of nanowires with different boundary conditions," *Applied Physics Letters*, vol. 93, p. 1240, 2008.
 - [11] K. F. Wang and B. L. Wang, "Effects of residual surface stress and surface elasticity on the nonlinear free vibration of nano-scale plates," *Journal of Applied Physics*, vol. 112, p. 1372, 2012.
 - [12] H. Yu, W. W. Zhang, S. Y. Lei, L. B. Lu, C. Sun, and Q. A. Huang, "Study on vibration behavior of doubly clamped silicon nanowires by molecular dynamics," *Journal of Nanomaterials*, vol. 2012, Article ID 342329, 6 pages, 2012.
 - [13] H. Zhan, Y. Gu, and H. S. Park, "Beat phenomena in metal nanowires, and their implications for resonance-based elastic property measurements," *Nanoscale*, vol. 4, no. 21, pp. 6779–6785, 2012.
 - [14] B. Liu, H. Zhang, J. Tao, Z. Liu, X. Chen, and Y. A. Zhang, "Development of a second-nearest-neighbor modified embedded atom method potential for silicon-phosphorus binary system," *Computational Materials Science*, vol. 120, pp. 1–12, 2016.
 - [15] B. J. Lee, W. S. Ko, H. K. Kim, and E. H. Kim, "The modified embedded-atom method interatomic potentials and recent progress in atomistic simulations," *Calphad-computer Coupling of Phase Diagrams & Thermochemistry*, vol. 34, no. 4, pp. 510–522, 2010.
 - [16] B.-J. Lee, "A modified embedded atom method interatomic potential for silicon," *Calphad*, vol. 31, no. 1, pp. 95–104, 2007.
 - [17] J. Schmidt, M. R. G. Marques, S. Botti, and M. A. L. Marques, "Recent advances and applications of machine learning in solid-state materials science," *npj Computational Materials*, vol. 5, no. 1, p. 83, 2019.
 - [18] T. Mueller, A. Hernandez, and C. Wang, "Machine learning for interatomic potential models," *The Journal of Chemical Physics*, vol. 152, no. 5, article 050902, 2020.
 - [19] C. L. Kuo and P. Clancy, "MEAM molecular dynamics study of a gold thin film on a silicon substrate," *Surface Science*, vol. 551, no. 1-2, pp. 39–58, 2004.
 - [20] D. D. Ma, C. S. Lee, F. C. Au, S. Y. Tong, and S. T. Lee, "Small-diameter silicon nanowire surfaces," *Science*, vol. 299, no. 5614, pp. 1874–1877, 2003.
 - [21] K. Chin-Lung and C. Paulette, "Development of atomistic MEAM potentials for the silicon–oxygen–gold ternary system," *Modelling & Simulation in Materials Science & Engineering*, vol. 13, no. 8, p. 1309, 2005.
 - [22] M. I. Baskes, "Modified embedded-atom potentials for cubic materials and impurities," *Physical Review B, Condensed Matter*, vol. 46, no. 5, pp. 2727–2742, 1992.
 - [23] S. Ryu, C. R. Weinberger, M. I. Baskes, and W. Cai, "Improved modified embedded-atom method potentials for gold and silicon," *Modelling and Simulation in Materials Science and Engineering*, vol. 17, no. 7, article 075008, 2009.
 - [24] J. R. Neighbours and G. A. Alers, "Elastic constants of silver and gold," *Physical Review*, vol. 111, no. 3, pp. 707–712, 1958.
 - [25] S. Ryu and W. Cai, "A gold-silicon potential fitted to the binary phase diagram," *Journal of Physics. Condensed Matter*, vol. 22, no. 5, article 055401, 2010.
 - [26] J. P. Perdew, A. Ruzsinszky, G. I. Csonka et al., "Restoring the density-gradient expansion for exchange in solids and surfaces," *Physical Review Letters*, vol. 100, no. 13, article 136406, 2008.
 - [27] G. Kresse and J. Furthmüller, "Efficient iterative schemes for *ab initio* total-energy calculations using a plane-wave basis set," *Physical Review B*, vol. 54, pp. 11169–11186, 1996.
 - [28] G. Kresse and J. Furthmüller, "Efficiency of *ab-initio* total energy calculations for metals and semiconductors using a plane-wave basis set," *Computational materials science*, vol. 6, no. 1, pp. 15–50, 1996.
 - [29] G. Kresse and J. Hafner, "Ab initio molecular dynamics for liquid metals," *Physical Review B: Condensed Matter*, vol. 47, no. 1, pp. 558–561, 1993.
 - [30] H.-S. Jang, D. Seol, and B.-J. Lee, "Modified embedded-atom method interatomic potential for the Mg-Zn-Ca ternary system," *Calphad*, vol. 67, article 101674, 2019.
 - [31] X. Dong, X. Fang, Y. Wang, and X. Song, "First-principles calculations of Au-supersaturated silicon formed by pulsed-laser irradiation," *Japanese Journal of Applied Physics*, vol. 58, no. 2, article 020904, 2019.
 - [32] M. R. Murty and H. A. Atwater, "Empirical interatomic potential for Si-H interactions," *Physical Review B*, vol. 51, no. 8, pp. 4889–4893, 1995.
 - [33] J. E. Northrup, "Structure of Si (100)H: dependence on the H chemical potential," *Physical Review B*, vol. 44, no. 3, pp. 1419–1422, 1991.
 - [34] B. I. Craig and P. V. Smith, "The structure of the Si(100)2 × 1: H surface," *Surface Science*, vol. 226, no. 1-2, pp. L55–L58, 1990.
 - [35] A. Bellec, N. Rompotis, and L. N. Kantorovich, "Dihydride dimer structures on the Si(100): H surface studied by low-temperature scanning tunneling microscopy," *Physical Review B*, vol. 78, no. 16, 2008.
 - [36] Y. J. Chabal, G. S. Higashi, K. Raghavachari, and V. A. Burrows, "Infrared spectroscopy of Si(111) and Si(100) surfaces after HF treatment: hydrogen termination and surface morphology," *Mrs Proceedings*, vol. 131, pp. 2104–2109, 1988.
 - [37] S. H. Lee and G. S. Hwang, "Diffusion and clustering of Au adatoms on H-terminated Si(111)-(1×1): A first principles study," *The Journal of Chemical Physics*, vol. 131, no. 14, article 144702, 2009.
 - [38] M. F. Ng, M. B. Sullivan, S. W. Tong, and P. Wu, "First-principles study of silicon nanowire approaching the bulk limit," *Nano Letters*, vol. 11, no. 11, pp. 4794–4799, 2011.

- [39] P. Liang, Y. Liu, H. Shu, Q. Dong, L. Wang, and T. Shen, "The influence of unintentional Au impurities on the doping properties of Si nanowires," *Solid State Communications*, vol. 183, pp. 8–12, 2014.
- [40] W.-H. Liang, X.-L. Wang, X.-C. Ding et al., "Stability and electronic structures of Au-doped silicon nanowires," *Acta Physico-Chimica Sinica*, vol. 27, no. 7, pp. 1615–1620, 2011.
- [41] J. E. Allen, E. R. Hemesath, D. E. Perea et al., "High-resolution detection of Au catalyst atoms in Si nanowires," *Nature Nanotechnology*, vol. 3, no. 3, pp. 168–173, 2008.
- [42] S. Plimpton, "Fast parallel algorithms for short-range molecular dynamics," *Journal of Computational Physics*, vol. 117, no. 1, pp. 1–19, 1995.
- [43] J. Zhang and C. Wang, "Beat vibration of hybrid boron nitride-carbon nanotubes - A new avenue to atomic-scale mass sensing," *Computational Materials Science*, vol. 127, pp. 270–276, 2017.
- [44] W. Weaver, S. Timoshenko, and D. H. Young, *vibration problems in engineering*, John Wiley & Sons, New York, ed. f. edition, 1990.
- [45] E. Gil-Santos, D. Ramos, J. Martínez et al., "Nanomechanical mass sensing and stiffness spectrometry based on two-dimensional vibrations of resonant nanowires," *Nature Nanotechnology*, vol. 5, no. 9, pp. 641–645, 2010.
- [46] A. K. Vallabhaneni, J. F. Rhoads, J. Y. Murthy, and X. Ruan, "Observation of nonclassical scaling laws in the quality factors of cantilevered carbon nanotube resonators," *Journal of Applied Physics*, vol. 110, p. 56, 2011.
- [47] G. Cao, Y. Chen, J. Jiao, and Y. Wang, "Harmonic behavior of silicon nanowire by molecular dynamics," *Mechanics Research Communications*, vol. 34, no. 5-6, pp. 503–507, 2007.